

# *New analytical solution and associated software for computing full-tensor gravitational field due to irregularly shaped bodies*

**Anita Thea Saraswati, Rodolphe Cattin,  
Stéphane Mazzotti & Cécilia Cadio**

**Journal of Geodesy**

Continuation of *Bulletin Géodésique*  
and *manuscripta geodaetica*

ISSN 0949-7714

J Geod

DOI 10.1007/s00190-019-01309-y



 Springer

**Your article is protected by copyright and all rights are held exclusively by Springer-Verlag GmbH Germany, part of Springer Nature. This e-offprint is for personal use only and shall not be self-archived in electronic repositories. If you wish to self-archive your article, please use the accepted manuscript version for posting on your own website. You may further deposit the accepted manuscript version in any repository, provided it is only made publicly available 12 months after official publication or later and provided acknowledgement is given to the original source of publication and a link is inserted to the published article on Springer's website. The link must be accompanied by the following text: "The final publication is available at [link.springer.com](http://link.springer.com)".**



# New analytical solution and associated software for computing full-tensor gravitational field due to irregularly shaped bodies

Anita Thea Saraswati<sup>1,2</sup> · Rodolphe Cattin<sup>1</sup> · Stéphane Mazzotti<sup>1</sup> · Cécilia Cadio<sup>1</sup>

Received: 17 October 2018 / Accepted: 9 October 2019  
 © Springer-Verlag GmbH Germany, part of Springer Nature 2019

## Abstract

We present a new analytical solution to compute the full-tensor gravity gradient due to a body mass of uniform density with arbitrary geometry. The solution is an extension of an existing analytical computation of gravitational anomalies of a polyhedron source, based on a transition of the general expressions from surface to line integrals. These developments enable the computation of the gravity gradient tensor using the same simple procedures as the gravitational field. The method is validated by comparing with a closed analytical solution, including on/in the near field of the body surface. The algorithm is implemented in the freely available MATLAB-based software called Gal Eötvös Earth Calculator. It is tested successfully for various measurement distances and body mass sizes, enabling applications from local geophysical prospecting to global topographic effect for satellite data. Due to its flexibility, the new solution, and the associated software, is particularly well suited for joint analyses of all types of gravity measurements regardless of the extent, altitude and irregularity of their spatial distribution.

**Keywords** Gravity · Gravity gradients · Analytical solution · Modelling · Algorithm

## 1 Introduction

The availability of gravity and gravity gradient datasets from ground measurements, airborne surveys and satellite missions allows the study of many phenomena such as water resource availability (Van Camp et al. 2017), volcanic activity (Jousset et al. 2003) or lithosphere dynamics (Cadio et al. 2016). The interpretation of these datasets requires calculating and modelling gravity and gravity gradient fields, taking into account the complex geometry of body masses from local to global scales including the curvature of the Earth.

At a global scale, spectral analysis is classically performed using spherical decomposition (Lee and Kaula 1967). This method is very efficient for uniform and global data coverage but becomes ineffective when measurements

are not regularly distributed or for regional application. These shortcomings can partly be overcome using wavelet decomposition, although it still requires refinements at resolution below 15 km (Chambodut et al. 2005; Panet et al. 2011). A second set of methods consists in dividing the anomalous body masses in a succession of finite elements, such as thin spherical layers (Tsoulis and Stary 2005), right rectangular prisms (e.g. Mader 1951; Nagy et al. 2000), inclined top and bottom faces of rectangular prisms (Tsoulis et al. 2003; D'Urso and Trotta 2015), triangular prisms (Woodward 1975), polygonal prisms (Smith 2000) or tesseraeoids (Grombein et al. 2013; Uieda et al. 2016).

An alternative technique, polyhedron modelling, is one of the most developed methods to perform gravimetric forward modelling due to its capacity to represent the geometry of arbitrary body masses (e.g. models of irregular buried masses or topography surface from digital elevation models). The advantage of polyhedron is thus that the shape of the modelled mass can be represented more precisely by using polygonal mesh to model the volume's surface, compared to an approximate geometry such as right rectangular prisms. Since the pioneer approaches developed by Hubbert (1948) or Talwani and Ewing (1960), several formulations have been proposed to calculate the gravity field due to an arbitrary polyhedron of

✉ Anita Thea Saraswati  
 anitatheasaraswati@gmail.com

<sup>1</sup> Géosciences Montpellier, UMR 5243, CNRS, Université de Montpellier, Place E. Bataillon, 34095 Montpellier Cedex 05, France

<sup>2</sup> Faculté des Science, de la Technologie et de la Communication, University of Luxembourg, Esch-sur-Alzette, Luxembourg

uniform density (e.g. Okabe 1979; Pohanka 1988; Werner and Scheeres 1997; Holstein 2002; Tsoulis 2012; D'Urso 2013, 2014). Among them, Singh and Guptasarma (2001) developed optimized formulations for the gravitational field of a polyhedron using Stokes' theorem, in which the surface integral over each polygonal facet of the polyhedron is converted into line integrals around its boundaries. Compared to previous approaches, these formulas are faster to compute because they do not require coordinate transformations, similar to Werner and Scheeres (1997) and Holstein (2002), and avoid the need to discriminate between observation points located outside, on the surface and inside the solid body.

In this paper, we present the expansion of the approach of Singh and Guptasarma (2001) extending the line integral analytical formulations to compute concurrently gravity and gravity gradients. In order to validate the method, we compare our results with the analytical solutions of a right rectangular prism proposed by Nagy et al. (2000). The implementation of these formulations is presented in the freely available MATLAB-based code *GEEC* (Gal Eötvös Earth Calculator) tailored for geophysics or geodesy applications. After we describe briefly the design of the software, we present some applications of *GEEC* to calculate a simple geometry buried mass and regional and global topography effects. We present a numerical investigation of the errors due to the body mass discretization and assess the dependency between optimum mesh size and the altitude of measurements.

## 2 Theory

This section develops the analytical solutions for the gravity  $g_\alpha$  and gravity gradients  $T_{\alpha\beta} = \delta g_\alpha / \delta g_\beta$  where  $\alpha, \beta \in \{x, y, z\}$  due to an irregular polyhedron body with a constant density in a right-handed 3D Cartesian system. The first section is a reminder of the main formulations obtained by Singh and Guptasarma (2001) to calculate the gravitational field. The second one is an extension of this previous work, in which we present formulas providing a new technique for computing concurrently all the components of both gravity and gravity gradients.

### 2.1 Line integral approach to calculate the gravitational field from an arbitrary polyhedron with a constant density

The component of gravity field  $g$  at a computation point  $O$  in the given direction  $\alpha \in \{x, y, z\}$  due to an arbitrary polyhedron with a constant density can be written as the surface integral (Singh and Guptasarma 2001)

$$g_\alpha(O) = G\rho \iint_s \frac{\alpha}{r^3} \mathbf{r} \cdot \mathbf{u}_i ds, \quad (1)$$

where  $G$  is the gravitational constant,  $\rho$  is the density of the body,  $\mathbf{r}$  is the position vector of a surface element  $ds$  with respect to the observation point  $O$ ,  $r$  is the Euclidean distance from the observation point  $O$  to a surface element of area  $ds$  on the surface of the body and  $\mathbf{u}_i$  is the unit outward normal vector at the surface element  $ds$  (Fig. 1).

The polyhedron is bounded by a number of plane facets; thus, the integration can be done separately on each facet. Summing the integration result over all the facets to obtain the attraction of the whole body, we get

$$g_\alpha(O) = G\rho \sum_i \mathbf{r} \cdot \mathbf{u}_i \iint_{S_i} \frac{\alpha}{r^3} ds, \quad (2)$$

where  $\mathbf{r}$  is the position vector of any vertex of the  $i$ th facet and  $\mathbf{u}_i$  is the unit outward normal vector of the  $i$ th facet. Let the  $i$ th facet have  $M$  vertices where the vector position of its  $k$ th vertex, be  $\mathbf{r}_{ik}$ , is ordered in counterclockwise direction seen from outside the body, the unit outward normal  $\mathbf{u}_i$  can be obtained by

$$\mathbf{u}_i = \frac{\mathbf{n}_i}{n_i}, \quad (3)$$

where  $\mathbf{n}_i = \sum_{k=2}^{M-1} (\mathbf{r}_{ik} - \mathbf{r}_{i1}) \times (\mathbf{r}_{i(k+1)} - \mathbf{r}_{i1})$  as illustrated in Fig. 1.  $n_i$  is the magnitude of  $\mathbf{n}_i$ .

As described in Guptasarma and Singh (1999), the surface integrals in Eq. (2) can be evaluated for each facet by converting them into line integrals of the edges that

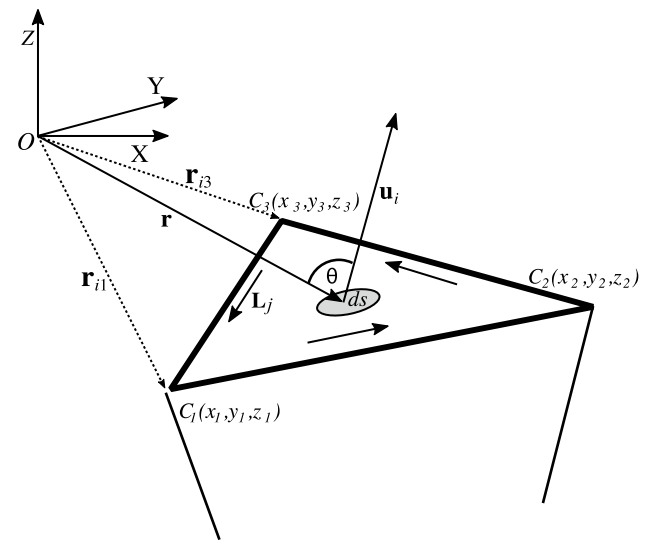


**Fig. 1** Polygonal surface in a right-handed Cartesian coordinate system and the scheme of the surface contribution computation.  $\mathbf{r}$  is the vector distance between the observation point  $O$  and the element centre.  $\mathbf{u}_i$  is the unit outward normal vector of the surface element  $ds$ .  $\mathbf{L}_j$  is the vector of the  $j$ th edge.  $\mathbf{r}_{ik}$  is the vector position of the vertex from the computation point. The small solid arrows show the direction of the line integration around the edges, counterclockwise from the outside.  $C_{ik}$  denotes the  $k$ th vertex of the  $i$ th surface

construct the facet. The approach is made by comparing the solution for the magnetic field from a polyhedron that can be written as

$$H_\alpha = - \sum_i \sigma_i \iint_{S_i} \frac{\alpha}{r^3} ds, \quad (4)$$

where  $\sigma_i$  is the surface pole density of the  $i$ th facet.

For unit pole density on the surface, the scalar integrals of the Cartesian component of the magnetic field over the  $i$ th polygon in Eq. (4) can be written as

$$H_{\alpha i} = \iint_{S_i} -\frac{\alpha}{r^3} ds. \quad (5)$$

Considering the magnetic field of the  $i$ th facet has a unit pole density, the inner product of the unit normal outward vector  $\mathbf{u}_i$  and the magnetic field  $H_i$ , with  $H_{xi}, H_{yi}, H_{zi}$  components, due to that facet is equal to  $\cos\theta/r^2 ds$ , where  $\theta$  is the angle between the position vector  $ds$  to the observation and the unit outward normal of  $ds$ .  $\cos\theta/r^2$  is also one of the existing solutions to obtain the solid angle subtended by a surface area  $ds$  at computation point  $O$  (cf., Thomas and Finley 1998; Van Oosterom and Strackee 2007).

Using the fact that, for the unit pole density, the solid angle  $\Omega_i$  subtended at the computation point by the  $i$ th facet is numerically equal to the component of the magnetic field  $H_{\alpha i}$  and parallel to the outward normal  $\mathbf{u}_i$ , we have

$$\Omega_i = lH_{xi} + mH_{yi} + nH_{zi}, \quad (6)$$

where  $(l, m, n)$  are the Cartesian components of  $\mathbf{u}_i$ . For a positive pole density, the field normal to the facet is away from the facet. As a consequence, the sign of  $\Omega_i$  would be the opposite of the sign of the scalar product of the outward vector  $\mathbf{u}_i$  and the vector position  $\mathbf{r}$  of any corner of the polygon with respect to the computation point  $O$  (Fig. 1).

Note that the surface integrals of the outward normal components of the curl are linearly related to the component of the field at the computation point. Taking the each component of the unit vector  $\mathbf{r}$  in the  $x, y, z$  directions as  $\mathbf{i}, \mathbf{j}, \mathbf{k}$ , we have

$$\begin{aligned} \mathbf{u}_i \cdot \operatorname{curl}\left(\frac{\mathbf{i}}{r}\right) &= \frac{ny - mz}{r^3}, \\ \mathbf{u}_i \cdot \operatorname{curl}\left(\frac{\mathbf{j}}{r}\right) &= \frac{lz - nx}{r^3}, \\ \mathbf{u}_i \cdot \operatorname{curl}\left(\frac{\mathbf{k}}{r}\right) &= \frac{mx - ly}{r^3}. \end{aligned} \quad (7)$$

Integrating these equations over the surface and combining with Eq. (5), we get

$$\begin{aligned} P_i &= \iint_{S_i} \mathbf{u}_i \cdot \operatorname{curl}\left(\frac{\mathbf{i}}{r}\right) ds = -nH_{yi} + mH_{zi}, \\ Q_i &= \iint_{S_i} \mathbf{u}_i \cdot \operatorname{curl}\left(\frac{\mathbf{j}}{r}\right) ds = nH_{xi} - lH_{zi}, \\ R_i &= \iint_{S_i} \mathbf{u}_i \cdot \operatorname{curl}\left(\frac{\mathbf{k}}{r}\right) ds = -mH_{xi} + lH_{yi}. \end{aligned} \quad (8)$$

By combining Eqs. (8) and (6) and noting that  $l^2 + m^2 + n^2 = 1$ , we obtain

$$\begin{aligned} H_{xi} &= l\Omega_i + nQ_i - mR_i, \\ H_{yi} &= m\Omega_i + lR_i - nP_i, \\ H_{zi} &= n\Omega_i + mP_i - lQ_i \end{aligned} \quad (9)$$

Inserting the combination of Eq. (5) and (9) into Eq. (2) and allowing for the fact that the components of gravity and magnetic fields have the same form, the solution of gravitational field using line integrals can be written as

$$\begin{aligned} g_x &= -G\rho \sum_i \mathbf{r} \cdot \mathbf{u}_i (l\Omega_i + nQ_i - mR_i), \\ g_y &= -G\rho \sum_i \mathbf{r} \cdot \mathbf{u}_i (m\Omega_i + lR_i - nP_i), \\ g_z &= -G\rho \sum_i \mathbf{r} \cdot \mathbf{u}_i (n\Omega_i + mP_i - lQ_i). \end{aligned} \quad (10)$$

According to Stokes' theorem, the surface integrals of the normal component of  $\operatorname{curl}(\mathbf{i}/r)$ ,  $\operatorname{curl}(\mathbf{j}/r)$ ,  $\operatorname{curl}(\mathbf{k}/r)$  are equal to the line integral of vector  $(\mathbf{i}/r)$ ,  $(\mathbf{j}/r)$  and  $\mathbf{k}/r$ , taken along the edges of the surface polygon in a counter-clockwise direction as seen from the outside of the polyhedron. The detail of the integration of the line integrals of  $(\mathbf{i}/r)$ ,  $(\mathbf{j}/r)$  and  $\mathbf{k}/r$  of each edge of a polygon is described in Guptasarma and Singh (1999).

In the solution using line integrals, the contributions of the  $j$ th edge  $P_{ij}, Q_{ij}, R_{ij}$  for the integration along the  $j$ th edge of the  $i$ th facet can be obtained from

$$P_{ij} = (I_j L_{jx})_i, \quad Q_{ij} = (I_j L_{jy})_i, \quad \text{and} \quad R_{ij} = (I_j L_{jz})_i. \quad (11)$$

Omitting the subscript  $i$ ,  $\mathbf{L}_j = (L_{jx}, L_{jy}, L_{jz}) = \mathbf{r}_{2j} - \mathbf{r}_{1j}$  are the Cartesian components of the vector along the  $j$ th edge, where  $\mathbf{r}_{2j}$  and  $\mathbf{r}_{1j}$  are the vertices' position of the end and the beginning of the evaluated edge. The length of the  $j$ th edge is  $L_j = |\mathbf{L}_j|$ . The line integral along edge  $I_j$  can be written as

$$I_j = \left( \frac{1}{L_j} \right) \ln \left[ \frac{\left( \sqrt{L_j^2 + b_j + r_j^2} + L_j + \frac{b_j}{2L_j} \right)}{\left( r_j + \frac{b_j}{2L_j} \right)} \right], \quad \text{if } \left( r_j + \frac{b_j}{2L_j} \right) \neq 0$$

and  $I_j = \left( \frac{1}{L_j} \right) \ln \left[ \frac{|L_j - r_j|}{r_j} \right], \quad \text{if } \left( r_j + \frac{b_j}{2L_j} \right) = 0,$

(12)

where

$$b_j = 2(\mathbf{r}_j \cdot \mathbf{L}_j)$$
(13)

and  $r_j$  is the Euclidean distance from the computation point to the beginning of  $j$ th edge.  $\mathbf{r}_j$  is the position vector of the beginning of the  $j$ th edge from the computation point  $O$ ; thus,  $(r_{jx}, r_{jy}, r_{jz})$  are the Cartesian coordinates of the vector  $\mathbf{r}_j$ . The condition of  $(r_j + (b_j/2L_j)) = 0$  is obtained where the observation point  $O$  is located on the  $j$ th edge or the observation point  $O$ , and the end and the beginning of the  $j$ th edge (in that order) are along a line. The beginning and the end of each edge are evaluated in a counterclockwise direction, seen from the outside.

Equations (11), (12) is not defined on points situated at a vertex of the polyhedron, resulting in  $r_j = 0$  if the computation is located at the beginning of the evaluated edge or  $L_j = r_j$  if the computation is located at the end of the evaluated edge. In this case, the contribution of the integral of  $1/r$  to the computed field goes infinity as  $\ln(x/0)$  or  $\ln(0)$ , respectively. However, this problem does not appear in the computation of the gravitational field, because it is omitted in the summation process indicated in Eq. (10), since  $\mathbf{r} \cdot \mathbf{u}_i = 0$ .

Thus, the total boundary contribution for each facet is the sum of the integral contribution of its edges is

$$P_i = \sum_j P_{ij}, \quad Q_i = \sum_j Q_{ij}, \quad R_i = \sum_j R_{ij}.$$
(14)

### 2.1.1 Computing solid angle

The solid angle  $\Omega_i$ , subtended by the computation point as the apex and each surface of the polygon, can be obtained by (Todhunter and Leathem 1949)

$$\Omega_i = \left( \sum_k \psi_{ik} \right) - (N_i - 2)\pi,$$
(15)

where  $\psi_{ik}$  is the angle between the planes forming the adjacent edge of the pyramid,  $k$  is the index of the common vertex of the adjacent edges of facet  $i$  and  $N$  is the number of the side of the  $i$ th facet (Fig. 2).

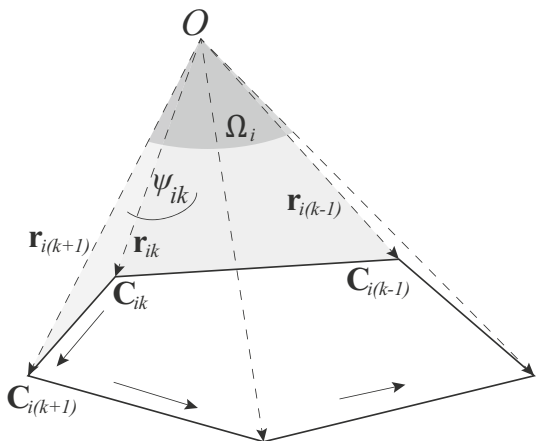


**Fig. 2** Solid angle of a facet  $\Omega$  (grey).  $\psi_{ik}$  is the angles between the planes forming the adjacent sides (light grey) between observation point  $O$  and the facets

The evaluation of the  $\psi_{ik}$  requires the position vector of three adjacent points,  $\mathbf{p}_1 = \mathbf{r}_{i(k-1)}$ ,  $\mathbf{p}_2 = \mathbf{r}_{ik}$ ,  $\mathbf{p}_3 = \mathbf{r}_{i(k+1)}$ , with the computation point  $O$  as the origin and in counterclockwise order seen from the outside. The angle  $\psi_{ik}$  is thus the angle between the planes  $OC_{i(k-1)}C_{ik}$  and  $OC_{ik}C_{i(k+1)}$ , intersecting along the line  $OC_{ik}$ .

The solid angle of the  $i$ th facet is negative ( $-\Omega_i$ ) if it is seen from the inside of the polyhedron. This can be recognized by taking the sign of the scalar product of  $\mathbf{u}_i \cdot \mathbf{p}_1$ . In this case, we change the order of the adjacent vertices to  $\mathbf{p}_1 = \mathbf{r}_{i(k+1)}$ ,  $\mathbf{p}_2 = \mathbf{r}_{ik}$ ,  $\mathbf{p}_3 = \mathbf{r}_{i(k-1)}$  for the evaluation of the  $\psi_{ik}$ .

Using the position vector of each corner of the facet to the computation point,

$$\mathbf{A}_1 = \frac{\mathbf{v}_1}{v_1} \quad \text{and} \quad \mathbf{A}_2 = \frac{\mathbf{v}_2}{v_2},$$
(16)

where  $\mathbf{v}_1 = \mathbf{p}_2 \times \mathbf{p}_1$  and  $\mathbf{v}_2 = \mathbf{p}_2 \times \mathbf{p}_3$ . Thus, for the evaluated adjacent angle, we have

$$\begin{cases} \psi_{ik} = \cos^{-1} (\mathbf{A}_1 \cdot \mathbf{A}_2) & \text{if } \mathbf{p}_3 \cdot \mathbf{A}_1 > 0 \\ \psi_{ik} = 2\pi - \cos^{-1} (\mathbf{A}_1 \cdot \mathbf{A}_2) & \text{if } \mathbf{p}_3 \cdot \mathbf{A}_1 < 0. \end{cases}$$
(17)

The sign of  $\mathbf{p}_3 \cdot \mathbf{A}_1$  can indicate whether this internal angle exceeds  $\pi$  or not. If the sign is negative, the internal angle at the  $j$ th corner exceeds  $\pi$ .

### 2.2 Analytical solution for the gravity gradients due to an arbitrary polyhedron

Following the approach described in the previous section, we extend the Guptasarma and Singh (1999) formulations to calculate all components of the gravity gradients. The partial derivatives of the gravity  $g_\alpha$ , known as the gravity gradients, at

the observation point  $O$  in direction  $\beta \in \{x, y, z\}$  can be written as

$$T_{\alpha\beta}(O) = \frac{\partial}{\partial \beta} g_\alpha(O), \alpha, \beta \in \{x, y, z\}. \quad (18)$$

Thus, the partial derivatives of Eq. (10) are

$$\begin{aligned} \frac{\partial g_x}{\partial \beta} &= -G\rho \sum_i \frac{\partial}{\partial \beta} \{ \mathbf{r} \cdot \mathbf{u}_i (l\Omega_i + nQ_i - mR_i) \}, \\ \frac{\partial g_y}{\partial \beta} &= -G\rho \sum_i \frac{\partial}{\partial \beta} \{ \mathbf{r} \cdot \mathbf{u}_i (m\Omega_i + lR_i - nP_i) \}, \\ \frac{\partial g_z}{\partial \beta} &= -G\rho \sum_i \frac{\partial}{\partial \beta} \{ \mathbf{r} \cdot \mathbf{u}_i (n\Omega_i + mP_i - lQ_i) \}. \end{aligned} \quad (19)$$

The position vector of any polyhedron vertex with respect to the observation point  $O(x_O, y_O, z_O)$  is defined as

$$\mathbf{r} = [r_x \ r_y \ r_z] = [x' - x_O \ y' - y_O \ z' - z_O], \quad (20)$$

where  $(x', y', z')$  is the Cartesian coordinate of the vertex. Analogous to the derivatives in Pohanka (1988) and Werner and Scheeres (1997), the partial derivative of the position vector  $\mathbf{r}$  evaluated at the observation point  $O$  is then

$$\left\{ \begin{array}{c} \frac{\partial}{\partial x} \\ \frac{\partial}{\partial y} \\ \frac{\partial}{\partial z} \end{array} \right\} \mathbf{r} = \left\{ \begin{bmatrix} -1 & 0 & 0 \\ 0 & -1 & 0 \\ 0 & 0 & -1 \end{bmatrix} \right\}. \quad (21)$$

By using the partial derivative of the vector position  $\mathbf{r}$  in Eq. (21), the result of the partial derivative of the scalar product  $\mathbf{r}$  and  $\mathbf{u}_i$  is

$$\frac{\partial}{\partial \beta} (\mathbf{r} \cdot \mathbf{u}_i) = -u_{i\beta}, \quad (22)$$

where  $u_{i\beta}$  is the scalar of the outward vector  $\mathbf{u}_i$  in the scalar component  $\beta$ . Combined with Eqs. (22), (19) can be therefore expanded into

$$\begin{aligned} \frac{\partial g_x}{\partial \beta} &= -G\rho \sum_i \left[ \left\{ \mathbf{r} \cdot \mathbf{u}_i \left( l \frac{\partial \Omega_i}{\partial \beta} + n \frac{\partial Q_i}{\partial \beta} - m \frac{\partial R_i}{\partial \beta} \right) \right\} - \{ u_{i\beta} (l\Omega_i + nQ_i - mR_i) \} \right] \\ \frac{\partial g_y}{\partial \beta} &= -G\rho \sum_i \left[ \left\{ \mathbf{r} \cdot \mathbf{u}_i \left( m \frac{\partial \Omega_i}{\partial \beta} + l \frac{\partial R_i}{\partial \beta} - n \frac{\partial P_i}{\partial \beta} \right) \right\} - \{ u_{i\beta} (m\Omega_i + lR_i - nP_i) \} \right] \\ \frac{\partial g_z}{\partial \beta} &= -G\rho \sum_i \left[ \left\{ \mathbf{r} \cdot \mathbf{u}_i \left( n \frac{\partial \Omega_i}{\partial \beta} + m \frac{\partial P_i}{\partial \beta} - l \frac{\partial Q_i}{\partial \beta} \right) \right\} - \{ u_{i\beta} (n\Omega_i + mP_i - lQ_i) \} \right]. \end{aligned} \quad (23)$$

The partial derivatives of  $P_i, Q_i, R_i$  and the solid angle  $\Omega_i$  of the  $i$ th facet are expanded in the following two steps.

## 2.2.1 Partial derivative of the solution of the line integral

Replacing  $t = \frac{\sqrt{L_j^2 + b_j + r_j^2} + L_j + \frac{b_j}{2L_j}}{r_j + \frac{b_j}{2L_j}}$  for  $\left(r_j + \frac{b_j}{2L_j}\right) \neq 0$  and  $t = \frac{|L_j - r_j|}{r_j}$  for  $\left(r_j + \frac{b_j}{2L_j}\right) = 0$  in Eq. (12), the partial derivatives of the solution of the line integral  $P, Q, R$  on each edge  $j$  of Eq. (11) are

$$\begin{aligned} \frac{\partial P_{ij}}{\partial \beta} &= \frac{L_{jx}}{L_j} \frac{1}{t} \frac{\partial t}{\partial \beta} \\ \frac{\partial Q_{ij}}{\partial \beta} &= \frac{L_{jy}}{L_j} \frac{1}{t} \frac{\partial t}{\partial \beta} \\ \frac{\partial R_{ij}}{\partial \beta} &= \frac{L_{jz}}{L_j} \frac{1}{t} \frac{\partial t}{\partial \beta}. \end{aligned} \quad (24)$$

To obtain  $\frac{\partial t}{\partial \beta}$ , we use the product rule

$$\frac{\partial t}{\partial \beta} = \frac{\left( \frac{\partial u}{\partial \beta} v - u \frac{\partial v}{\partial \beta} \right)}{v^2} \quad (25)$$

with  $u = \sqrt{L_j^2 + b_j + r_j^2} + L_j + \frac{b_j}{2L_j}$  and  $v = r_j + \frac{b_j}{2L_j}$  for  $\left(r_j + \frac{b_j}{2L_j}\right) \neq 0$ . We have

$$\frac{\partial u}{\partial \beta} = \frac{1}{2} \frac{1}{\sqrt{L_j^2 + b_j + r_j^2}} \frac{\partial}{\partial \beta} (L_j^2 + b_j + r_j^2) + \frac{1}{2L_j} \frac{\partial b_j}{\partial \beta} \quad (26)$$

and

$$\frac{\partial v}{\partial \beta} = \frac{\partial r_j}{\partial \beta} + \frac{1}{2L_j} \frac{\partial b_j}{\partial \beta}. \quad (27)$$

The derivative of  $b_j$  in Eq. (13) is

$$\frac{\partial b_j}{\partial \beta} = \frac{\partial}{\partial \beta} (2(\mathbf{r}_j \cdot \mathbf{L}_j)) = -2L_{j\beta}, \quad (28)$$

and the derivative of  $r_j$  is

$$\frac{\partial r_j}{\partial \beta} = \frac{\partial}{\partial \beta} (\sqrt{r_{jx}^2 + r_{jy}^2 + r_{jz}^2}) = \frac{1}{2} \frac{1}{r_j} (-2r_{j\beta}) = -\frac{r_{j\beta}}{r_j}; \quad (29)$$

thus, we have

$$\frac{\partial r_j^2}{\partial \beta} = 2r_j \frac{\partial r_j}{\partial \beta} = -2r_{j\beta}. \quad (30)$$

Substituting Eqs. (28), (29) and (30) in Eqs. (26) and (27),

$$\frac{\partial u}{\partial \beta} = -\left( \frac{L_{j\beta} + r_{j\beta}}{\sqrt{L_j^2 + b_j + r_j^2}} + \frac{L_{j\beta}}{L_j} \right) \quad (31)$$

and

$$\frac{\partial v}{\partial \beta} = -\left( \frac{r_{j\beta}}{r_j} + \frac{L_{j\beta}}{L_j} \right). \quad (32)$$

If  $\left(r_j + \frac{b_j}{2L_j}\right) = 0$ , we substitute  $u = |L_j - r_j|$  and  $v = r_j$ ; thus, we obtain

$$\frac{\partial u}{\partial \beta} = \frac{(L_j - r_j)}{|L_j - r_j|} \frac{\partial}{\partial \beta} (L_j - r_j) = \frac{(L_j - r_j)}{|L_j - r_j|} \frac{L_{j\beta}}{L_j} \quad (33)$$

and

$$\frac{\partial v}{\partial \beta} = \frac{r_{j\beta}}{r_j}. \quad (34)$$

For points situated at a vertex of the polyhedron, the contribution of  $\partial I_j/\partial \beta$  to the second-order derivatives goes infinity as the result of  $x/0$ . However, this problem does not appear in the computation of the gravity gradients, because it is omitted in the summation process indicated in Eq. (23), since  $\mathbf{r} \cdot \mathbf{u}_i = 0$ .

### 2.2.2 Partial derivative of the solid angle

Replacing  $\mathbf{A}_1 \cdot \mathbf{A}_2$  with  $B$  of Eq. (17), the derivative of the angle of the  $i$ th facet at the  $k$ th vertex can be written

$$\begin{cases} \frac{\partial}{\partial \beta} \psi_{ik} = \frac{\partial}{\partial \beta} \cos^{-1} B = -\frac{1}{\sqrt{1-B^2}} \frac{\partial B}{\partial \beta} & \text{if } \mathbf{p}_3 \cdot \mathbf{A}_1 > 0 \\ \frac{\partial}{\partial \beta} \psi_{ik} = \frac{1}{\sqrt{1-B^2}} \frac{\partial B}{\partial \beta} & \text{if } \mathbf{p}_3 \cdot \mathbf{A}_1 < 0, \end{cases} \quad (35)$$

where

$$\frac{\partial B}{\partial \beta} = \left( \frac{\partial \mathbf{A}_1}{\partial \beta} \cdot \mathbf{A}_2 \right) + \left( \mathbf{A}_1 \cdot \frac{\partial \mathbf{A}_2}{\partial \beta} \right). \quad (36)$$

To obtain the derivative of  $\mathbf{A}_1$  and  $\mathbf{A}_2$ , first we calculate the derivative of  $\mathbf{v}_1$ ,  $\mathbf{v}_2$  and its magnitude  $v_1$ ,  $v_2$ ,

$$\begin{Bmatrix} \frac{\partial}{\partial x} \\ \frac{\partial}{\partial y} \\ \frac{\partial}{\partial z} \end{Bmatrix} \mathbf{v}_1 = \begin{Bmatrix} \frac{\partial}{\partial x} \\ \frac{\partial}{\partial y} \\ \frac{\partial}{\partial z} \end{Bmatrix} (\mathbf{p}_2 \times \mathbf{p}_1) = \begin{Bmatrix} [0 \ (p_1 - p_2)\mathbf{k} \ (p_2 - p_1)\mathbf{j}] \\ [(p_2 - p_1)\mathbf{k} \ 0 \ (p_1 - p_2)\mathbf{i}] \\ [(p_1 - p_2)\mathbf{j} \ (p_2 - p_1)\mathbf{i} \ 0] \end{Bmatrix} \quad (37)$$

$$\begin{Bmatrix} \frac{\partial}{\partial x} \\ \frac{\partial}{\partial y} \\ \frac{\partial}{\partial z} \end{Bmatrix} \mathbf{v}_2 = \begin{Bmatrix} \frac{\partial}{\partial x} \\ \frac{\partial}{\partial y} \\ \frac{\partial}{\partial z} \end{Bmatrix} \begin{Bmatrix} [0 \ (p_3 - p_2)\mathbf{k} \ (p_2 - p_3)\mathbf{j}] \\ [(p_2 - p_3)\mathbf{k} \ 0 \ (p_3 - p_2)\mathbf{i}] \\ [(p_3 - p_2)\mathbf{j} \ (p_2 - p_3)\mathbf{i} \ 0] \end{Bmatrix} \quad (38)$$

and

$$\begin{aligned} \frac{\partial}{\partial \beta} v_1 &= \frac{\partial}{\partial \beta} \left( \sqrt{v_{1x}^2 + v_{1y}^2 + v_{1z}^2} \right) \\ &= \frac{1}{2} \frac{1}{\sqrt{v_{1x}^2 + v_{1y}^2 + v_{1z}^2}} \frac{\partial}{\partial \beta} (v_{1x}^2 + v_{1y}^2 + v_{1z}^2) \\ &= \frac{1}{2} \frac{1}{v_1} \left( 2v_{1x} \frac{\partial v_{1x}}{\partial \beta} + 2v_{1y} \frac{\partial v_{1y}}{\partial \beta} + 2v_{1z} \frac{\partial v_{1z}}{\partial \beta} \right) \\ &= \frac{1}{v_1} \left( \mathbf{v}_1 \cdot \frac{\partial \mathbf{v}_1}{\partial \beta} \right). \end{aligned} \quad (39)$$

Similarly for the derivative of  $v_2$

$$\frac{\partial}{\partial \beta} v_2 = \frac{\partial}{\partial \beta} \left( \sqrt{v_{2x}^2 + v_{2y}^2 + v_{2z}^2} \right) = \frac{1}{v_2} \left( \mathbf{v}_2 \cdot \frac{\partial \mathbf{v}_2}{\partial \beta} \right). \quad (40)$$

Using Eqs. (37) to (40) to obtain the derivatives of  $\mathbf{A}_1$  and  $\mathbf{A}_2$ , we have

$$\frac{\partial \mathbf{A}_1}{\partial \beta} = \frac{\partial}{\partial \beta} \left( \frac{\mathbf{v}_1}{v_1} \right) = \frac{1}{v_1^2} \left( \frac{\partial \mathbf{v}_1}{\partial \beta} v_1 - \mathbf{v}_1 \frac{\partial}{\partial \beta} v_1 \right) \quad (41)$$

and

$$\frac{\partial \mathbf{A}_2}{\partial \beta} = \frac{\partial}{\partial \beta} \left( \frac{\mathbf{v}_2}{v_2} \right) = \frac{1}{v_2^2} \left( \frac{\partial \mathbf{v}_2}{\partial \beta} v_2 - \mathbf{v}_2 \frac{\partial}{\partial \beta} v_2 \right). \quad (42)$$

Finally, using the result of Eq. (35), the derivative of the solid angle of the  $i$ th facet can be obtained with

$$\frac{\partial}{\partial \beta} \Omega_i = \sum_k \frac{\partial}{\partial \beta} \psi_{ik}. \quad (43)$$

### 3 Numerical assessment

We assess the numerical performance of our new solution, including the first and second derivatives of potential, by computing the attraction of a right rectangular prism and comparing with the analytical solution (e.g. Mader 1951; Nagy et al. 2000). A prism with a dimension of  $1 \times 1 \times 1 \text{ m}^3$  with a constant density  $\rho = 1000 \text{ kg m}^{-3}$  is used ( $G = 6.67408 \times 10^{-11} \text{ m}^3 \text{ kg}^{-1} \text{ s}^{-2}$ ). The prism is modelled as a polyhedron source

consisting in six rectangular facets, as shown in Fig. 3, with  $x$ ,  $y$  and  $z$  in the east, north and up directions.

The computation is performed on the same level as the top surface of the prism, with a grid distribution of  $0.1 \times 0.1$  m. The results are documented in Fig. 4. Compared to the analytical solution of Nagy et al. (2000), our numerical computations reach the level of precision limited by the internal MATLAB 16 digits of precision. The results in Fig. 4 (left) demonstrate the numerical consistency of the approach and indicate that the numerical method does not meet any difficulty from singularities at specific positions, i.e. the prism corners and edges and the internal facet surface. The numerical stability of the

method can also be characterized in function of angular extent  $\gamma$  of the body (Holstein and Ketteridge 1996; Holstein et al. 1999), where  $\gamma = d/r$ ;  $d$  is the typical linear dimension of the mass body and  $r$  is the typical distance between the observation point and the mass body. For the gravity computation, the level of agreement between our method and the analytical solution of a prism is  $10^{-19}$ – $10^{-23}$  in function of the increasing angular extent  $\gamma$  (Table 4 in Appendix 1).

The gravity gradients are continuous at every point in the vicinity of which the density function and its partial derivatives are continuous (Tychonov and Samarski 1964). This means that the gravity gradients can have discontinuity at points that belong to the boundary surface of the polyhedron (Kellogg 1967; Torge 2001; Hofmann-Wellenhof and Moritz 2005). This condition is also stated and discussed in Nagy et al. (2000), Tsoulis (2012) and D'Urso (2014). Thus, for the numerical assessment of the computation of gravity gradients, the computations are set outside the boundary surface. The observation points are set 0.01 m above the top surface of the prism with the same grid space as the calculation of the gravitational field. The results of the computation and the comparison with Nagy et al. (2000) analytical solution are presented in Fig. 5. The maximum discrepancies are less than  $2 \times 10^{-19}$  s $^{-2}$ , in agreement with MATLAB numerical precision. The sum of the diagonal components of the gravity gradients is smaller than  $1.1 \times 10^{-21}$  s $^{-2}$ , showing that the numerical computation fulfils Laplace's equation. Unlike the results from Tsoulis

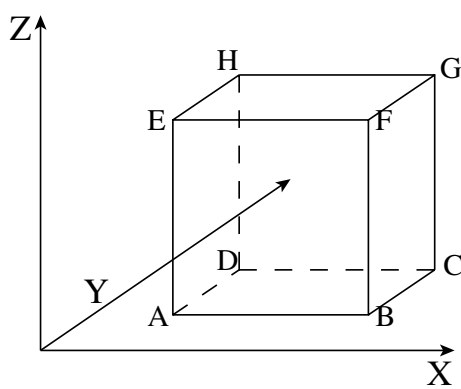


**Fig. 3** A right rectangular prismatic body as a tested polyhedral source

**Fig. 4** Comparison of gravitational field computed on the  $h$  = top surface of the prism between the results of the presented method and analytical solutions of a rectangular prism by Nagy et al. (2000). **a** Gravitational field from the presented solution. **b** Gravitational field from prism analytical solution. **c** Discrepancies between two methods

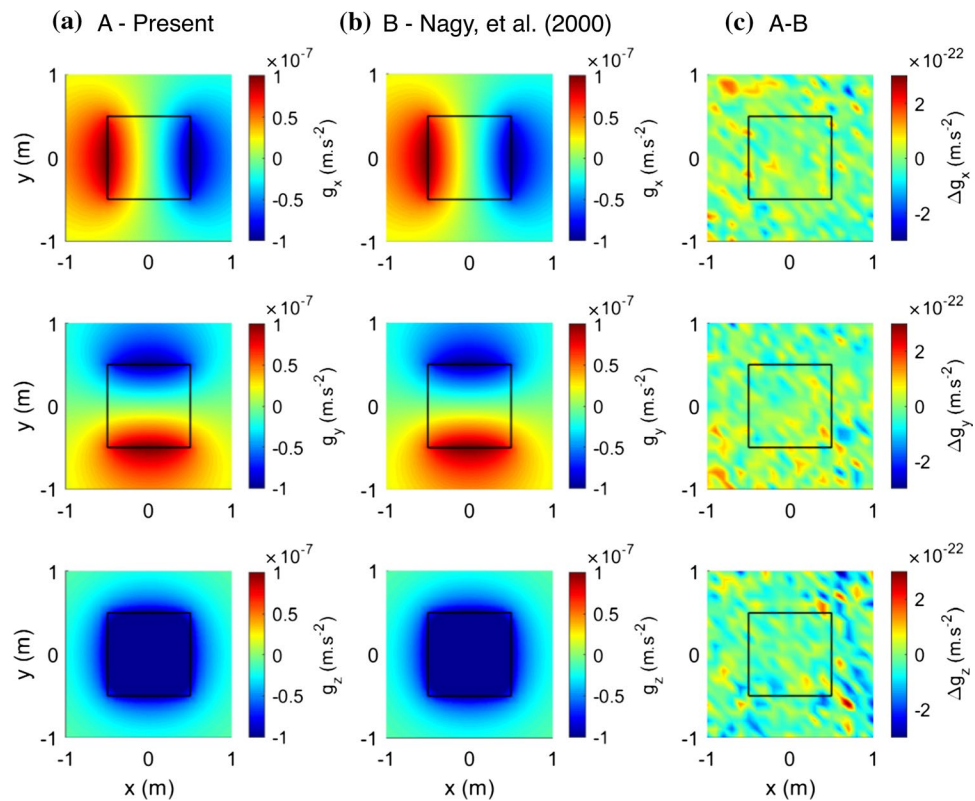
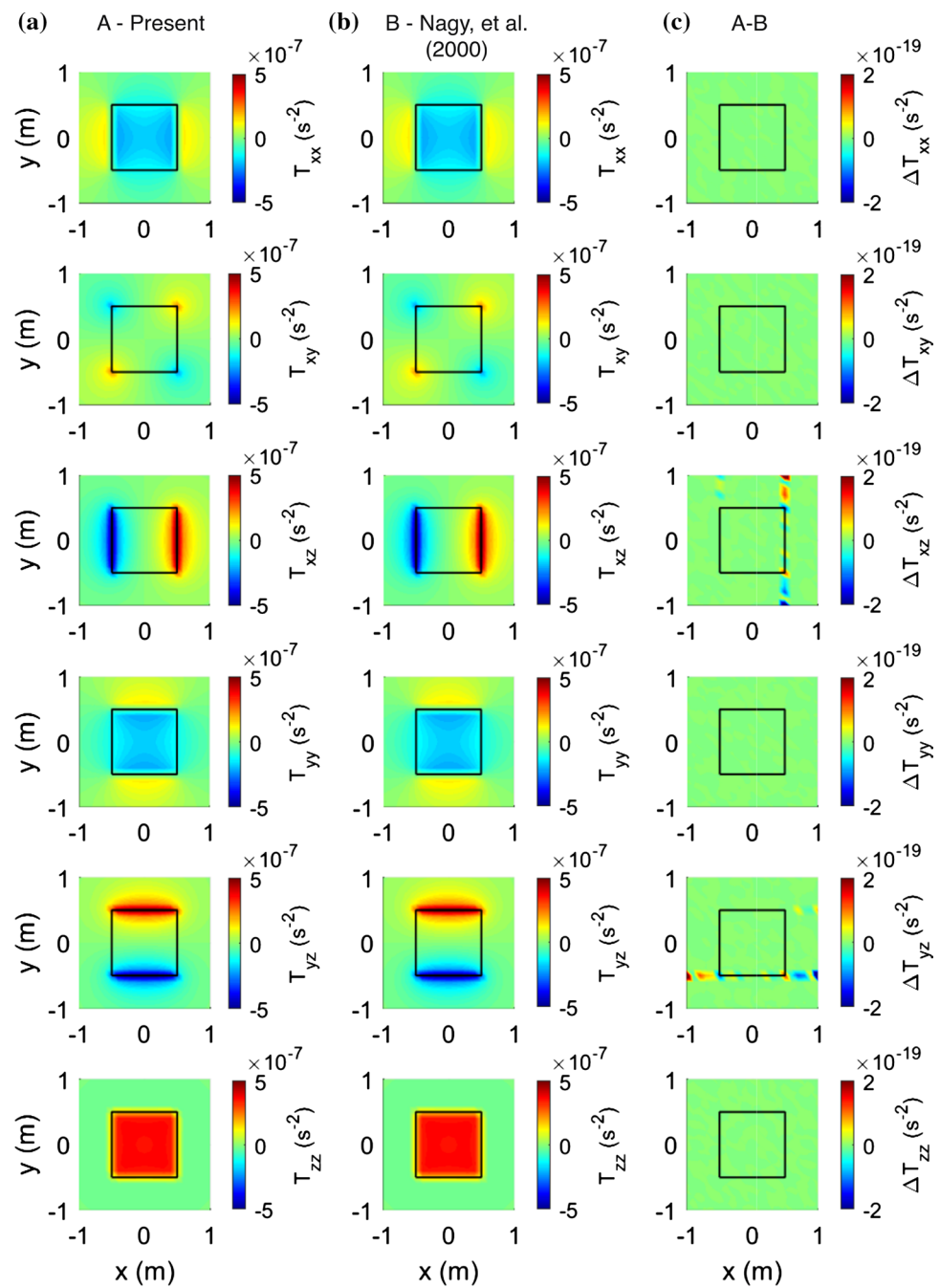


**Fig. 5** Comparison of gravity gradients computed on 0.01 m above of the prism's top surface between the results of the presented method and analytical solutions of a rectangular prism by Nagy et al. (2000). **a** Gravity gradients from the presented method. **b** Gravity gradients from prism analytical solution. **c** Discrepancies between two methods



(2012), there is no singularity produced in the method when the observation point is located outside of the polyhedron.

#### 4 Implementation and applications

We implement the line integral approach to compute both the gravity and gravity gradients in the open-source software *GEEC* (freely available online on the web page of Geosciences Montpellier laboratory, <http://www.gm.univ-montp2.fr>). An archived version of the source code is also available

as part of this paper. We take advantage of the MATLAB Parallel Computing Toolbox to enhance the computation time. Commonly, ground gravity measurements as well as satellite and airborne observation points are spatially unevenly distributed. We allow for this type of data with computation points that can be defined at any location without any interpolation in the calculation process. Computation points can be defined either as gridded or scattered locations given in a geographical coordinate system (longitude, latitude and altitude).

The body mass is modelled as polyhedron with polygonal facets with a counterclockwise sense of the vertices seen from

the outside of the body. Triangular mesh is recommended, due to its robust representation of any specific geometry (Tsoulis 2003). The polyhedron geometric topology is required either provided as external information or computed internally. An ellipsoidal approximation is used to avoid errors due to neglecting the Earth curvature (Tsoulis et al. 2009). The computation reference system (vertical datum) is flexible (geoid or ellipsoid) in order to avoid indirect effects caused by differences in the vertical reference level (Talwani 1998).

Very convenient software such as IGMAS (e.g. Götze and Lahmeyer 1988) already exists; however, it provides calculation on planar surface. In the following, we apply our approach to very local to global scales by taking into account the curvature of the Earth. We present the comparison with simple analytical solutions and results obtained with *Tesseroids* (Uieda et al. 2016). The results of the numerical computation in this section are presented in mGal for gravity and Eötvös for gravity gradients ( $1 \text{ mGal} = 10^{-5} \text{ m s}^{-2}$ ,  $1 \text{ E} = 10^{-9} \text{ s}^{-2}$ ).

#### 4.1 Anomaly due to a buried sphere

A first example application consists in modelling the gravity and gravity gradients due to a buried body. Such a computation

is very common to interpret gravity anomalies in geophysical prospecting, which requires forward modelling to image oil pockets, ore veins or water reservoirs. The scale associated with these local studies is often small, less than a few kilometres. We compare the computed gravity and gravity gradients due to a buried sphere (Fig. 6) with the analytical solution

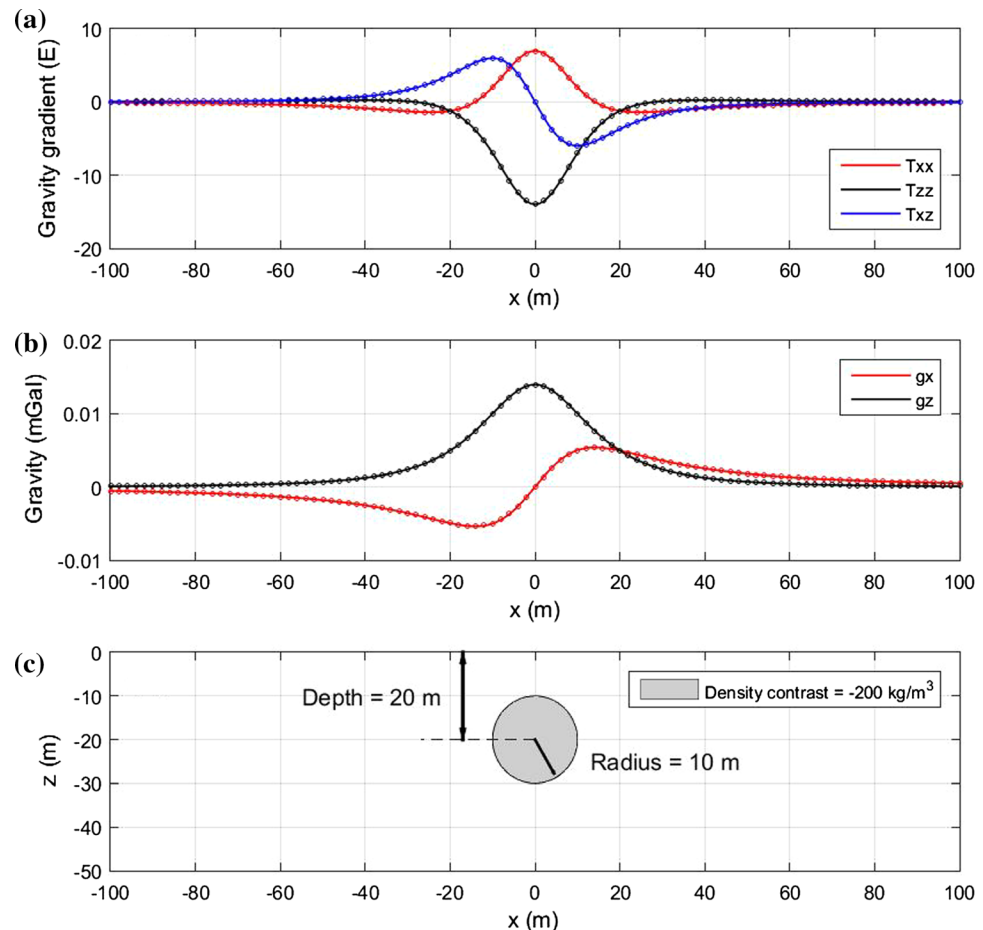
$$g_x = \frac{ax}{(x^2 + z^2)^{\frac{3}{2}}} \quad \text{and} \quad g_z = \frac{az}{(x^2 + z^2)^{\frac{3}{2}}} \quad (44)$$

with  $a = \frac{-4\pi GR^3 \Delta\rho}{3}$ ,

and

$$\begin{aligned} T_{xx} &= \frac{\partial g_x}{\partial x} = \frac{a}{(x^2 + z^2)^{\frac{3}{2}}} \left( 1 - \frac{3x^2}{x^2 + z^2} \right), \\ T_{zz} &= \frac{\partial g_z}{\partial z} = \frac{a}{(x^2 + z^2)^{\frac{3}{2}}} \left( 1 - \frac{3z^2}{x^2 + z^2} \right), \\ T_{xz} &= \frac{\partial g_x}{\partial z} = -3a \frac{xz}{(x^2 + z^2)^{\frac{5}{2}}}, \end{aligned} \quad (45)$$

**Fig. 6** GEEC vs. theoretical analytical solutions for surface gravity and gravity gradients due to a buried sphere of anomalous density. **a** Gravity gradients from the theoretical (solid line) and GEEC (circles) solutions. **b** Gravity from the theoretical solutions. **c** Body mass geometry



where  $x$  and  $z$  are the horizontal and vertical distance from the sphere centre.  $z$  is positive upward.  $R$  is the sphere radius and  $\Delta\rho$  the density contrast. We assume a sphere with a radius of 10 m, a density contrast of  $-200 \text{ kg m}^{-3}$ , centred at 20 m depth. For our computation, the surface of the sphere is discretized using a mesh size (distance between triangle vertices) of 0.3 m.

Compared with the standard deviations of both ground gravity and gravity gradient measurements (Van Camp et al. 2017), our computation results are in very good agreement with the theoretical values obtained along a surface profile (Fig. 6). The maximum differences are less than  $7.5 \times 10^{-5}$  mGal and 0.06 E for the gravity and gravity gradients, respectively. This very simple application demonstrates the robustness of our approach at a local scale and its relevance to assess the geometry and density contrast of a buried body using forward modelling.

## 4.2 Effect of a superficial Earth's shell at various measurement heights

Since the computation is performed using planar facets to discretize the surface of the arbitrary mass body, the smaller the mesh size, the better the geometry, but the longer the computation time and memory requirements, preventing calculations at too high resolution on a large or global scale. To overcome this limitation, one can define an optimum mesh size as the model resolution required to achieve a given accuracy. This optimum mesh size depends on both the size of the body mass and the measurement height, which also can represent the distance of the body mass to the measurement points.

To evaluate the relationship between height of measurement and model resolution, and also its implication on the computation time, we compute the vertical attractions  $g_z$  and  $T_{zz}$  due to a spherical shell with a mass density  $\rho=2670 \text{ kg m}^{-3}$  and a constant thickness of 1 km above a reference sphere with a mean radius  $R=6378.137 \text{ km}$ . This simple example represents a test case of a standard Bouguer plateau correction of the topography in gravity studies.

**Table 1** Gravitation  $g_z$  and gravity gradient  $T_{zz}$  due to a 1-km-thick spherical shell with a constant density  $\rho=2670 \text{ kg m}^{-3}$  above a reference sphere with a mean radius  $R=6378.137 \text{ km}$

$h$ (km)	Analytical solution		GEEC solution			
	$g_z$ (mGal)	$T_{zz}$ (mE)	High resolution (5 km)		Low resolution (150 km)	
			$g_z$ (mGal)	$T_{zz}$ (mE)	$g_z$ (mGal)	$T_{zz}$ (mE)
On surface	223.895	701.960	223.880	494.187	223.036	358.943
2	223.825	701.630	223.821	649.811	222.999	369.583
5	223.615	700.641	223.614	699.869	222.884	401.080
10	223.265	698.998	223.265	698.996	222.670	450.898
255	207.076	624.369	207.076	624.369	207.029	624.230

Analytical and numerical GEEC results are calculated at various computation altitude  $h$  ranging from 0 to 255 km. GEEC computation is performed with a mesh size of 5 and 150 km (see Fig. 7)

We test heights of observation points between the ground surface and 255 km of altitude. The accuracy results are defined as the absolute difference with the theoretical values obtained from Eqs. (44) and (45) for two concentric spheres of differing radii:

$$\begin{cases} \Delta g_\alpha = g_\alpha(R + 1\text{km}) - g_\alpha(R) \\ \Delta T_{\alpha\beta} = T_{\alpha\beta}(R + 1\text{km}) - T_{\alpha\beta}(R), \end{cases} \quad (46)$$

where  $\alpha, \beta \in \{x, y, z\}$ .

The reference values for the spherical shell at each computation altitude  $h$  are indicated in Table 1. As expected, for any computation altitude, our results show that the error is inversely proportional to the resolution of the model (Table 1 and Fig. 7). For instance, the ground-based  $g_z$  errors are 15  $\mu\text{Gal}$  and 859  $\mu\text{Gal}$  for a mesh size of 5 km and 150 km, respectively. The error also depends on the considered altitude (Fig. 7). Assuming a low-resolution sphere model (i.e. mesh size of 150 km), the  $g_z$  error decreases from 859 to 47  $\mu\text{Gal}$  with an increase in altitude from 0 to 255 km (Table 1).

In order to achieve an accuracy (approximation of the exact analytical values) of 99.9%, a resolution ca. 35 km is required for near surface gravity calculations, whereas a resolution ca. 80 km is sufficient at 10 km altitude, and all tested resolutions (up to 150 km) are adequate for satellite altitude (Fig. 7a). For the gravity gradient (Fig. 7b), an accuracy of 99.9% requires a minimum resolution ca. 15 km for airborne surveys (10 km altitude) and is always achieved for satellite altitudes. In contrast to the gravity signal, a 99.9% accuracy in the gradient is not achieved using any tested resolution for any altitude below 5 km. These results are consistent with those obtained by Uieda et al. (2016), showing that  $T_{zz}$  requires higher surface resolution than  $g_z$  to obtain the same percentage of error.

The detail of the computational effort is given in Table 5 and Fig. 12 in Appendix 2. The CPU time and the number of facets exhibit a nearly linear relation  $t = 1.2 \times 10^{-5} * n_{\text{facet}}$ . Computation time increases very strongly from 20 s to 9 min for mesh sizes ranging from 25 to 5 km. These results demonstrate the efficiency of GEEC to compute both gravity

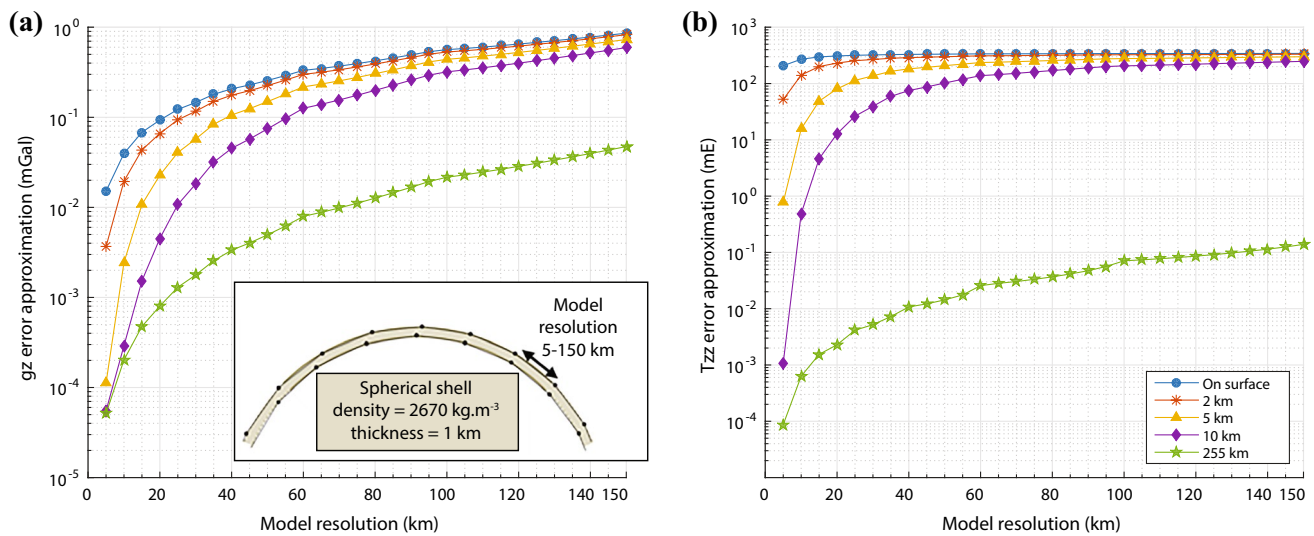


**Fig. 7** Relationship between height of gravity measurements and optimum mesh size (model resolution). Inset: Diagram of the model geometry used in *GEEC* to compute the gravity effect of a spherical shell with a constant density of  $2670 \text{ kg.m}^{-3}$  and a thickness of 1 km,

corresponding to a plateau covering the whole Earth. **a** Error in  $g_z$  by *GEEC* computation relative to the analytical solution, as a function of the model resolution and the measurement height. **b** Same as **a** for  $T_{zz}$  error

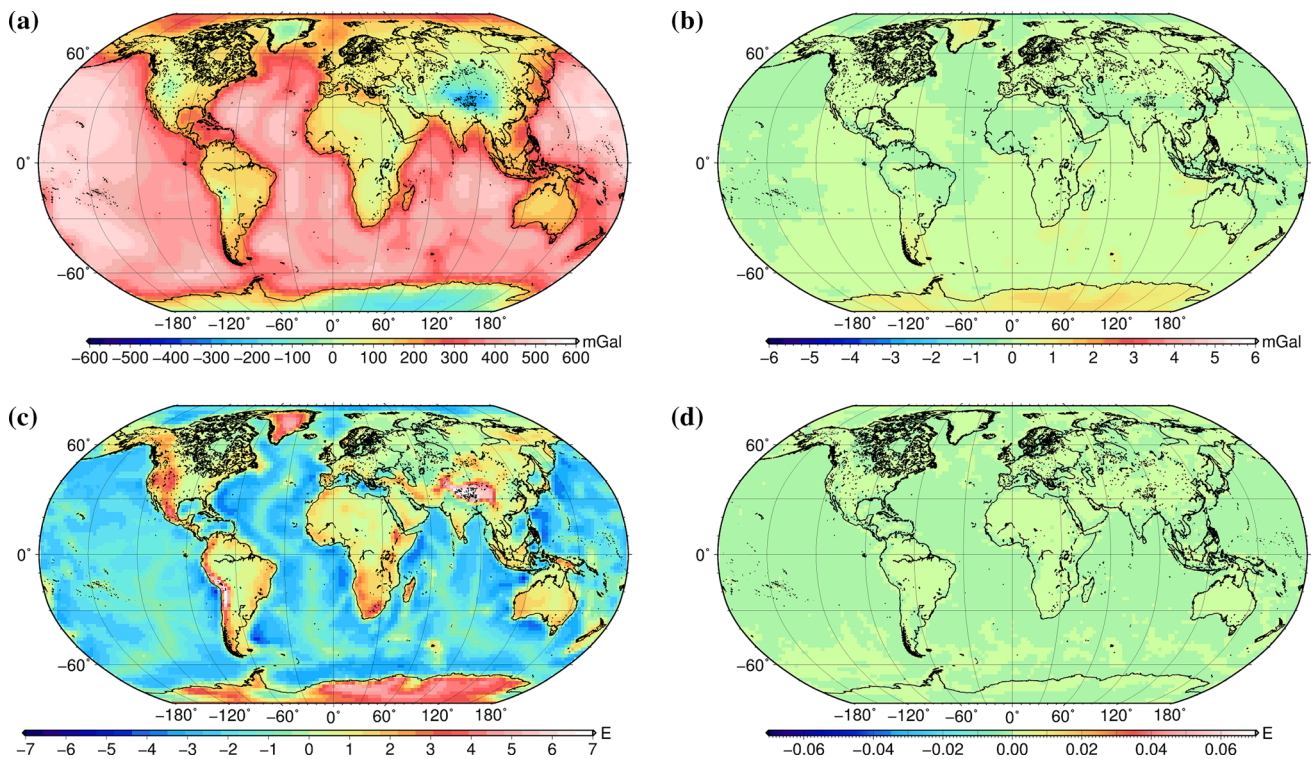


**Fig. 8** Comparison between *GEEC* and *Tesseroids* softwares. **a** and **c** Calculated  $g_z$  and  $T_{zz}$  due to global topography effect using *GEEC* at 255 km computation height with a model resolution of 10 km. Note that a positive mass contrast has a negative effect in vertical gravity

the ENU system. **b** and **d** Differences between *GEEC* and *Tesseroids* computations. Note the colour scale, which represents 1% of the colour scale in (a) and (c)

and gravity gradients at 255 km, allowing a comparison with the dense and global GOCE dataset. The presented approach is also suitable for studying regional airborne surveys (5–10 km altitude). In contrast, ground or low-altitude airborne surveys (<2 km) require a mode resolution higher than ca. 5 km, for which a global-scale computation can be impractical. If the extent of surveys is local (few 10 s km), our approach remains relevant. As in the case of a buried sphere, a small network extent makes it possible to improve the resolution without increasing computing times too much.

### 4.3 Global and regional topographic effect

The last application consists in the computation of the topography contribution in the gravity field, which is an important step to assess deep sources from gravitational data. We compare the computed gravity and gravity gradients due to topography and bathymetry with results obtained from the software *Tesseroids* (Uieda et al. 2016), in which the Earth topography is discretized in tesseroids. We use the DTM2006.0 data defined on a grid of 5' × 5' (Pavlis et al. 2007). On the basis of the results obtained in the previous section, we recompose DTM2006.0 in a 10 km equidistant mesh, providing a uniform resolution over the entire Earth. For the computation using *Tesseroids*, we deactivate the adaptive discretization to keep the original grid size. In both cases, we decompose the topographic model in two

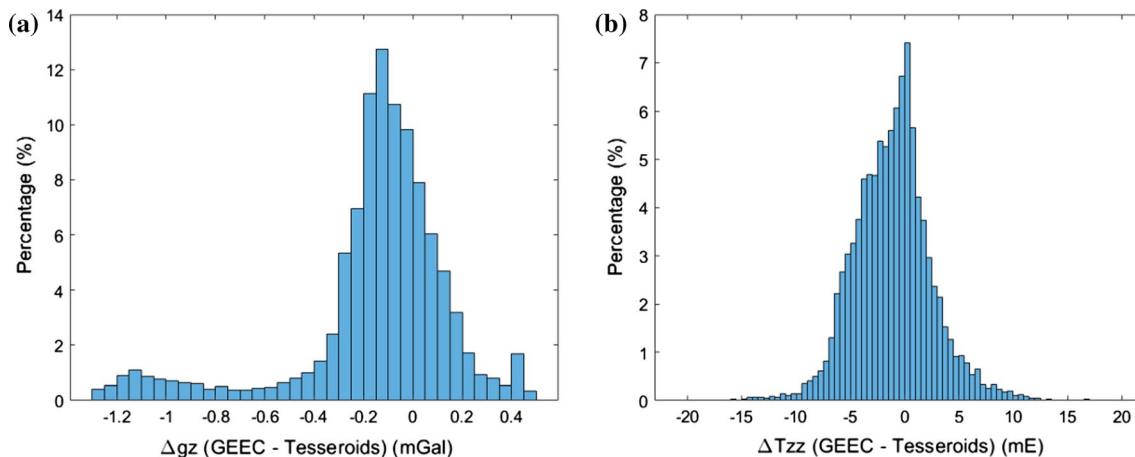
**Table 2** Statistic properties of the discrepancy between global topography effect computed by *GEEC* and *Tesseroids* (Uieda et al. 2016)

	Min	Max	Std
$\Delta g_z$ (mGal)	-1.296	0.487	0.314
$\Delta T_{zz}$ (mE)	-20.941	19.965	3.608

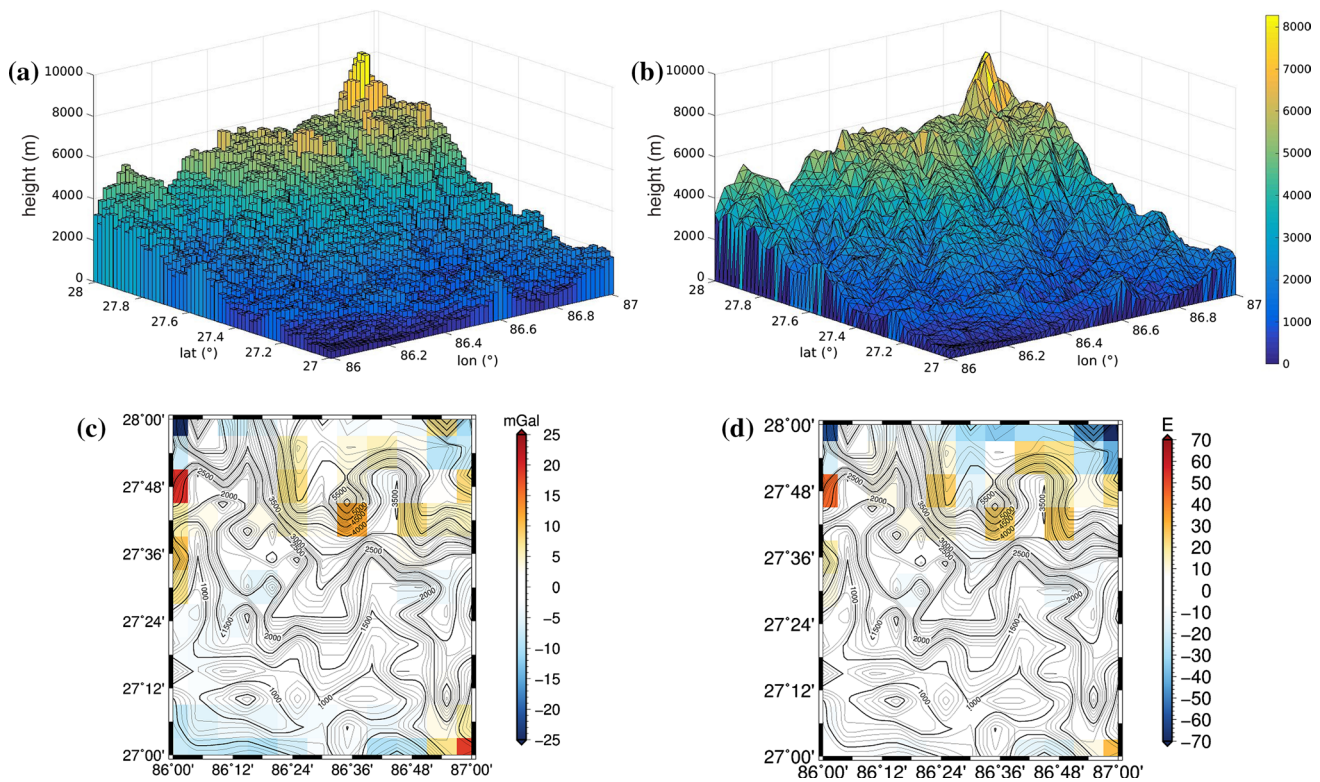
parts: a rock layer for masses above sea level with a density  $\rho_c = 2670 \text{ kg m}^{-3}$  and a water layer for masses below sea level with a density  $\rho_w = 1000 \text{ kg m}^{-3}$ . Using the crustal density as the reference density, this gives a density contrast for the ocean of  $-1670 \text{ kg m}^{-3}$ . For simplicity, the ice layer above sea level is considered as a rock layer. We set the computation points on a  $2^\circ \times 2^\circ$  grid at 255 km of ellipsoid height, which corresponds to the mean altitude of the GOCE mission (Rummel et al. 2011).

Figure 8 shows the gravity  $g_z$  and gradient  $T_{zz}$  topographic effects computed with *GEEC* (Fig. 8a and c) and their respective differences with the *Tesseroids* computation (Fig. 8b and d). *GEEC* and *Tesseroids* give very consistent results. Their differences are in the range of GOCE measurement uncertainties, i.e. 1 mGal and 10–60 mE for gravity and gravity gradient, respectively (Bruinsma et al. 2013; Panet et al. 2014). For  $g_z$ , maximum differences are ca.  $\pm 1.3$  mGal, less than 0.25% of the topographic effect (Table 2). For  $T_{zz}$ , the maximum differences are  $\pm 21$  mE with an overall standard deviation of 3.6 mE. The distributions of the discrepancies between the two methods are presented in Fig. 9.

Most of the large discrepancies are located in high-latitude areas, such as Antarctica and Greenland. The first reason is the difference between the meshing techniques in the two softwares. In *GEEC*, we use a homogeneous topography model with a resolution of 10 km, while for *Tesseroids*, the topography is modelled on a geographical grid where the grid size varies with the latitude. This leads to distortions of the tesseroid shapes from nearly rectangular at the equator to nearly triangular at the poles, which results in inaccurate computations in the tesseroid approach (Grombein et al. 2013). Second, the geometry of the mass distribution and the computation points are



**Fig. 9** Distribution of the discrepancy of global topography effect in **a**  $g_z$  (in mGal) and **b**  $T_{zz}$  (in mE) between the result from *GEEC* and *Tesseroids* (Uieda et al. 2016) computation



**Fig. 10** Effect of the discretization method in a rugged topographic surface, such as in the Himalayas of eastern Nepal. We consider an airborne survey at a constant altitude of 10 km. **a** Topographic sur-

face discretization using prisms or tesseroids elements. **b** Same as **a** with a polyhedrons approach. **c** and **d** Difference in  $g_z$  and  $T_{zz}$  calculated from these two methods

on the sphere in the *Tesseroids* software, whereas they are given on the ellipsoid in *GEEC*. This results in larger differences in the mass measurement distance at high latitudes. The high topographies in Antarctica and Greenland amplify these factors.

Beyond these differences due to global meshing, the discrepancy between our calculations and *Tesseroids* results can also be associated with the two different techniques used to model the local topography surface. To highlight this point, we compare the polyhedron and tesseroid approaches at a regional scale over the Himalaya of eastern Nepal (86–87°E and 27–28°N) for a computation height of 10 km and grid size of 0.1° (Fig. 10). The topography model is DTM2006.0 with a grid resolution of 5' (~ 10 km) and global topography extension, which corresponds to ca. 6,000,000 computation points. We obtain local deviations up to 20 mGal and 60 E in high-slope areas (cf. Table 3 and Fig. 11). Unsurprisingly, our approach is more suitable to model a rugged topography: the triangle-shaped discretization results in smaller deviations from the actual

**Table 3** Statistic properties of the discrepancy of the computation results by *GEEC* and *Tesseroids* (Uieda et al. 2016) on Himalaya region at a computation altitude of 10 km above ellipsoid

	Min	Max	Std
$\Delta g_z$ (mGal)	-24.271	19.659	5.495
$\Delta T_{zz}$ (E)	-45.401	69.482	15.114

geometry where the slope and geometry variations can be well preserved and modelled and less computation biases, compared to the rectangle-shaped discretization used in *Tesseroids* (Tsoulis 2003).

This application validates the use of *GEEC* to compute gravity and gravity gradients at regional and global scales. Compared to rectangular prism and tesseroid approaches, our approach gives consistent results but provides a more flexible way to preserve the roughness of the Earth's surface in topography modelling.

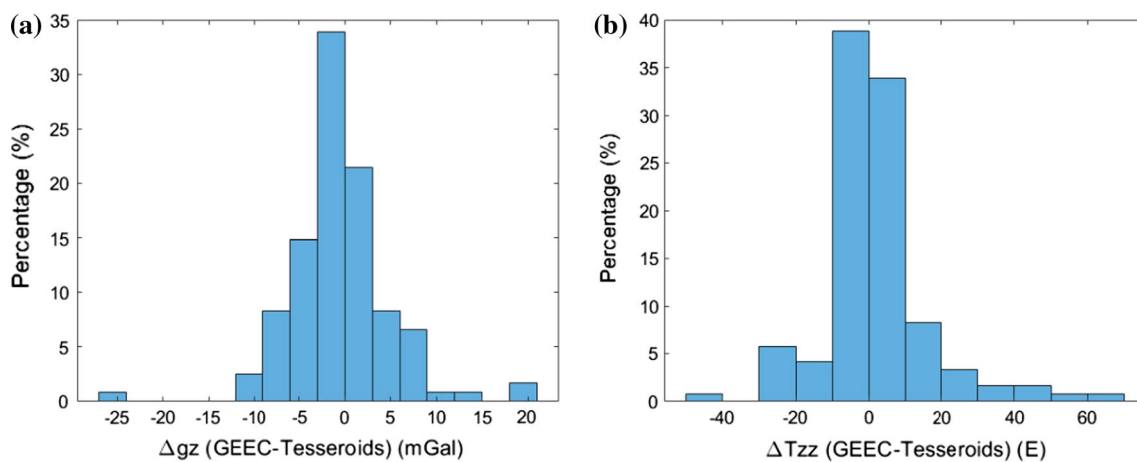


**Fig. 11** Distribution of the discrepancy of topography effect calculation on Himalaya region in **a**  $g_z$  (in mGal) and **b**  $T_{zz}$  (in mE) between the result from *GEEC* and *Tesseroids* (Uieda et al. 2016) computation. The computations are performed at an altitude of 10 km above ellipsoid

## 5 Conclusion

In this paper, we present new formulas for gravity gradients based on the analytical solutions of the expansion of the line integrals of a constant-density polyhedron body, following the analytical solution for the gravitational field by Singh and Guptasarma (2001). Our solutions do not require coordinate transformations, which allows faster computations. The fact that the formulas can be applied to any general polygonal shape makes this method flexible for a wide range of applications. We show that the developed formulas are robust and accurate.

The solution is implemented in an open-source tool *GEEC* (Gal Eötvös Earth Calculator) to perform forward modelling of gravity and gravity gradients of an irregular body mass discretized in polyhedron. This MATLAB-based software allows detailed modelling of bodies with complex surfaces at any input model size and resolution. Several applications are presented, including the calculation of gravity and gravity gradients for (1) local ground surveys as typically performed for exploration geophysics, (2) the global analysis of a spherical shell taking into account the curvature of the Earth and (3) the assessment of global and regional topography effects at satellite and airborne altitudes. The results demonstrate the robustness of our approach and provide a means to better assess the mesh size required to

achieve a targeted accuracy, which depends on both the size of the body mass and its distance to the measurement points. Although a regular meshing is suitable for high measurement heights ( $> 5$  km) such as airborne surveys and satellite data, grid refinement is needed for low-altitude measurements in the immediate vicinity of the computation point.

Compared to alternative approaches, the two main advantages of our new solution lie in the capacity (1) to preserve the complexity of the body mass geometries at all scales and (2) to compute concurrently gravity and gravity gradients for any measurement points regardless of the extent and irregularity of their spatial distribution. This solution is thus well suited for developments of joint inversions of all type of gravity measurements.

**Acknowledgements** This work was supported by Grants from Beaasiswa Unggulan (BU) of Indonesian Ministry of Education and Culture, Campus France Agence nationale de la recherche (ANR) Grant ANR-12-CHEX-0004-01 and CNES TOSCA. The authors acknowledge the comments and helpful suggestions of the editor and three anonymous reviewers that helped to improve the manuscript.

## Appendix 1

See Table 4.

**Table 4** Comparisons between polyhedron analytical formulation and right rectangular prism for points situated outside the attracting prism

	$\gamma$	A. GEEC	B. Nagy et al. (2000)	A-B	$\sum T_{\alpha\beta}, \alpha = \beta$
$10^{-1}$	$g_x (\text{ms}^{-2})$	-3.801289E-08	-3.801289E-08	1.124966E-22	8.621936E-22
	$g_y (\text{ms}^{-2})$	-3.801289E-08	-3.801289E-08	3.970467E-23	
	$g_z (\text{ms}^{-2})$	-3.801289E-08	-3.801289E-08	5.955700E-23	
	$T_{xx} (\text{s}^{-2})$	3.311437E-22	7.408518E-24	3.237351E-22	
	$T_{xy} (\text{s}^{-2})$	7.395213E-08	7.395213E-08	5.029258E-22	
	$T_{xz} (\text{s}^{-2})$	7.395213E-08	7.395213E-08	4.235165E-22	
	$T_{yy} (\text{s}^{-2})$	2.696609E-22	7.408518E-24	2.622524E-22	
	$T_{yz} (\text{s}^{-2})$	7.395213E-08	7.395213E-08	4.367514E-22	
	$T_{zz} (\text{s}^{-2})$	2.613891E-22	7.408518E-24	2.539806E-22	
	$g_x (\text{ms}^{-2})$	-5.714086E-09	-5.714086E-09	-5.128520E-23	-1.809458E-22
	$g_y (\text{ms}^{-2})$	-5.714086E-09	-5.714086E-09	-5.128520E-23	
	$g_z (\text{ms}^{-2})$	-5.714086E-09	-5.714086E-09	-6.617445E-23	
	$T_{xx} (\text{s}^{-2})$	-5.831623E-23	-1.111278E-23	-4.720346E-23	
	$T_{xy} (\text{s}^{-2})$	3.818228E-09	3.818228E-09	-4.880366E-23	
	$T_{xz} (\text{s}^{-2})$	3.818228E-09	3.818228E-09	-6.286573E-23	
$10^0$	$T_{yy} (\text{s}^{-2})$	-6.141816E-23	-1.111278E-23	-5.030538E-23	
	$T_{yz} (\text{s}^{-2})$	3.818228E-09	3.818228E-09	-6.286573E-23	
	$T_{zz} (\text{s}^{-2})$	-6.121137E-23	-1.111278E-23	-5.009859E-23	
	$g_x (\text{ms}^{-2})$	-1.164825E-10	-1.164825E-10	1.017691E-21	4.499976E-23
	$g_y (\text{ms}^{-2})$	-1.164825E-10	-1.164825E-10	3.656655E-22	
	$g_z (\text{ms}^{-2})$	-1.164825E-10	-1.164825E-10	3.656655E-22	
	$T_{xx} (\text{s}^{-2})$	5.451637E-23	3.704259E-24	5.081211E-23	
	$T_{xy} (\text{s}^{-2})$	1.109359E-11	1.109359E-11	-5.328045E-23	
	$T_{xz} (\text{s}^{-2})$	1.109359E-11	1.109359E-11	-3.621823E-23	
	$T_{yy} (\text{s}^{-2})$	-4.761135E-24	3.704259E-24	-8.465394E-24	
	$T_{yz} (\text{s}^{-2})$	1.109359E-11	1.109359E-11	-3.620692E-23	
	$T_{zz} (\text{s}^{-2})$	-4.755481E-24	3.704259E-24	-8.459740E-24	
$10^1$	$g_x (\text{ms}^{-2})$	-1.271473E-12	-1.271473E-12	-1.938547E-20	-2.620515E-22
	$g_y (\text{ms}^{-2})$	-1.271473E-12	-1.271473E-12	-2.537157E-20	
	$g_z (\text{ms}^{-2})$	-1.271473E-12	-1.271473E-12	-2.537157E-20	
	$T_{xx} (\text{s}^{-2})$	-4.783854E-23	-7.408518E-24	-4.043003E-23	
	$T_{xy} (\text{s}^{-2})$	1.265147E-14	1.265147E-14	-1.728951E-23	
	$T_{xz} (\text{s}^{-2})$	1.265147E-14	1.265147E-14	-4.053700E-23	
	$T_{yy} (\text{s}^{-2})$	-1.071064E-22	-7.408518E-24	-9.969790E-23	
	$T_{yz} (\text{s}^{-2})$	1.265147E-14	1.265147E-14	-4.053700E-23	
	$T_{zz} (\text{s}^{-2})$	-1.071065E-22	-7.408518E-24	-9.969802E-23	
$10^2$	$g_x (\text{ms}^{-2})$	-1.282942E-14	-1.282975E-14	3.254603E-19	2.297571E-22
	$g_y (\text{ms}^{-2})$	-1.282942E-14	-1.282975E-14	5.033833E-19	
	$g_z (\text{ms}^{-2})$	-1.282930E-14	-1.282975E-14	4.441152E-19	
	$T_{xx} (\text{s}^{-2})$	-2.219456E-23	0	-2.219456E-23	
	$T_{xy} (\text{s}^{-2})$	1.282293E-17	1.282284E-17	8.580961E-23	
	$T_{xz} (\text{s}^{-2})$	1.282296E-17	1.282284E-17	1.145269E-22	
	$T_{yy} (\text{s}^{-2})$	1.556099E-22	0	1.556099E-22	
	$T_{yz} (\text{s}^{-2})$	1.282296E-17	1.282284E-17	1.145269E-22	
	$T_{zz} (\text{s}^{-2})$	9.634173E-23	0	9.634173E-23	

The five cases listed here express a gradual increase in the angular extent  $\gamma$  between the same prism and the computation point

## Appendix 2

See Fig. 12 and Table 5.

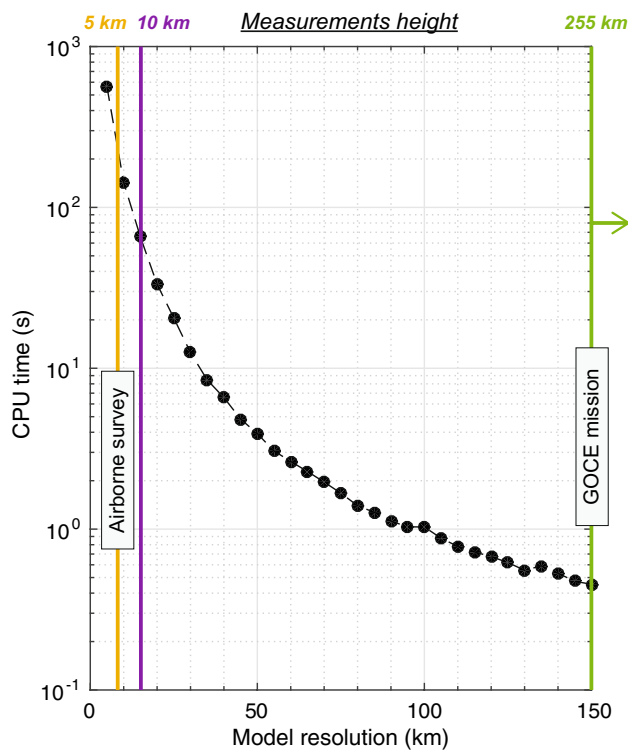


**Fig. 12** Relationship between CPU computation time, model resolution and measurement heights. Black circles are related to simulations performed using a computer with CPU Intel Xeon Processor E5, 3.20 GHz processor base frequency, with 8 cores and 16 threads per core (see Table 2). Vertical colour lines are associated with optimum model resolutions assuming an accuracy of 99.9% for the calculated gravity and gravity gradients. Colour text gives measurement heights. Note that ground and low-altitude airborne surveys require mesh resolutions smaller than 5 km

**Table 5** Computation time as a function of model resolution (see Fig. 12)

Resolution (km)	Number of point	Number of facet	CPU time (s)
5	23,611,683	47,117,844	560.4783
10	5,902,922	11,779,460	142.8204
15	2,623,522	5,235,316	65.5157
20	1,475,732	2,944,866	33.2904
25	944,469	1,884,714	20.5205
30	655,882	1,308,828	12.5056
35	481,873	961,588	8.4574
40	368,935	736,216	6.5717
45	291,504	581,702	4.8327
50	236,119	471,178	3.9219
55	195,140	389,404	3.0618
60	163,972	327,208	2.6336
65	139,716	278,804	2.2824
70	120,470	240,398	1.9610
75	104,943	209,412	1.6734
80	92,235	184,054	1.3990
85	81,703	163,038	1.2719
90	72,878	145,426	1.1223
95	65,408	130,520	1.0331
100	59,031	117,794	1.0316
105	53,543	106,844	0.8780
110	48,786	97,350	0.7806
115	44,637	89,070	0.7215
120	40,995	81,802	0.6747
125	37,781	75,388	0.6198
130	34,931	69,700	0.5547
135	32,391	64,634	0.5910
140	30,119	60,100	0.5319
145	28,078	56,026	0.4740
150	26,237	52,354	0.4542

The number of vertex and facet of each model are included. All of the simulations in this study are performed using a computer with CPU Intel Xeon Processor E5, 3.20 GHz processor base

## References

- Bruinsma SL, Förste C, Abrikosov O et al (2013) The new ESA satellite-only gravity field model via the direct approach. *Geophys Res Lett.* <https://doi.org/10.1002/grl.50716>
- Cadio C, Saraswati A, Cattin R, Mazzotti S (2016) A new approach to assess isostatic compensation of topography in continental domain from GOCE gravity gradients. *Geophys J Int.* <https://doi.org/10.1093/gji/ggw281>
- Chambodut A, Panet I, Mandea M et al (2005) Wavelet frames: an alternative to spherical harmonic representation of potential fields. *Geophys J Int* 163:875–899. <https://doi.org/10.1111/j.1365-246X.2005.02754.x>
- D'Urso MG (2013) On the evaluation of the gravity effects of polyhedral bodies and a consistent treatment of related singularities. *J Geod* 87:239–252. <https://doi.org/10.1007/s00190-012-0592-1>
- D'Urso MG (2014) Analytical computation of gravity effects for polyhedral bodies. *J Geod* 88:13–29. <https://doi.org/10.1007/s00190-013-0664-x>
- D'Urso MG, Trotta S (2015) Comparative assessment of linear and bilinear prism-based strategies for terrain correction computations. *J Geod* 89:199–215. <https://doi.org/10.1007/s00190-014-0770-4>
- Götze H-J, Lahmeyer B (1988) Application of three-dimensional interactive modeling in gravity and magnetics. *Geophysics* 53:1096–1108. <https://doi.org/10.1190/1.1442546>
- Grombein T, Seitz K, Heck B (2013) Optimized formulas for the gravitational field of a tesseroid. *J Geod* 87:645–660. <https://doi.org/10.1007/s00190-013-0636-1>
- Guptasarma D, Singh B (1999) New scheme for computing the magnetic field resulting from a uniformly magnetized arbitrary polyhedron. *Geophysics* 64:70–74. <https://doi.org/10.1190/1.1444531>
- Hofmann-Wellenhof B, Moritz H (2005) Physical geodesy. Springer, Berlin
- Holstein H (2002) Gravimagnetic similarity in anomaly formulas for uniform polyhedra. *Geophysics* 10(1190/1):1500373
- Holstein H, Ketteridge B (1996) Gravimetric analysis of uniform polyhedra. *Geophysics* 61:357–364. <https://doi.org/10.1190/1.1443964>
- Holstein H, Schürholz P, Starr AJ, Chakraborty M (1999) Comparison of gravimetric formulas for uniform polyhedra. *Geophysics* 64:1438–1446. <https://doi.org/10.1190/1.1444648>
- Hubbert MK (1948) A line-integral method of computing the gravimetric effects of two-dimensional masses. *Geophysics* 13:215–225. <https://doi.org/10.1190/1.1437395>
- Jouset P, Mori H, Okada H (2003) Elastic models for the magma intrusion associated with the 2000 eruption of Usu Volcano. *J Volcanol Geotherm Res, Hokkaido.* [https://doi.org/10.1016/S0377-0273\(03\)00090-8](https://doi.org/10.1016/S0377-0273(03)00090-8)
- Kellogg OD (1967) Foundations of potential theory. Springer, Berlin
- Lee WHK, Kaula WM (1967) A spherical harmonic analysis of the Earth's topography. *J Geophys Res* 72:753–758. <https://doi.org/10.1029/JZ072i002p00753>
- Mader K (1951) Das Newtonsche Raumpotential prismatischer Körper und seine Ableitungen bis zur 3. Ordnung Österr Z f, Vermessungswesen, p 11
- Nagy D, Papp G, Benedek J (2000) The gravitational potential and its derivatives for the prism. *J Geod* 74:552–560. <https://doi.org/10.1007/s001900000116>
- Okabe M (1979) Analytical expressions for gravity anomalies due to homogeneous polyhedral bodies and translations into magnetic anomalies. *Geophysics* 44:730–741. <https://doi.org/10.1190/1.1440973>
- Panet I, Kuroishi Y, Holschneider M (2011) Wavelet modelling of the gravity field by domain decomposition methods: an example over Japan. *Geophys J Int* 184:203–219. <https://doi.org/10.1111/j.1365-246X.2010.04840.x>
- Panet I, Pajot-Métivier G, Greff-Lefftz M et al (2014) Mapping the mass distribution of Earth's mantle using satellite-derived gravity gradients. *Nat Geosci* 7:131–135. <https://doi.org/10.1038/ngeo2063>
- Pavlis NK, Factor JK, Holmes SA (2007) Terrain-related gravimetric quantities computed for the next EGM. In: Proceedings of 1st international symposium on international gravity field service (IGFS), Istanbul 318–323
- Pohanka V (1988) Optimum expression for computation of the gravity field of a homogeneous polyhedral body1. *Geophys Prospect* 36:733–751. <https://doi.org/10.1111/j.1365-2478.1988.tb02190.x>
- Rummel R, Yi W, Stummer C (2011) GOCE gravitational gradiometry. *J Geod* 85:777–790. <https://doi.org/10.1007/s00190-011-0500-0>
- Singh B, Guptasarma D (2001) New method for fast computation of gravity and magnetic anomalies from arbitrary polyhedra. *Geophysics* 66:521–526. <https://doi.org/10.1190/1.1444942>
- Smith DA (2000) The gravitational attraction of any polygonally shaped vertical prism with inclined top and bottom faces. *J Geod* 74:414–420. <https://doi.org/10.1007/s001900000102>
- Talwani M (1998) Errors in the total Bouguer reduction. *Geophysics* 63:1125–1130. <https://doi.org/10.1190/1.1444412>
- Talwani M, Ewing M (1960) Rapid computation of gravitational attraction of three-dimensional bodies of arbitrary shape. *Geophysics* 25:203–225. <https://doi.org/10.1190/1.1438687>
- Thomas GBJ, Finley RL (1998) Calculus and analytic geometry. Addison-Wesley Publishing Company, Boston
- Todhunter I, Leathem JG (1949) Spherical Trigonometry. Macmillan and co., limited, London
- Torge W (2001) Geodesy. Walter de Gruyter, Berlin
- Tsoulis D (2003) Terrain modeling in forward gravimetric problems: a case study on local terrain effects. *J Appl Geophys.* <https://doi.org/10.1016/j.jappgeo.2003.09.001>
- Tsoulis D (2012) Analytical computation of the full gravity tensor of a homogeneous arbitrarily shaped polyhedral source using line integrals. *Geophysics* 77:F1–F11. <https://doi.org/10.1190/geo2010-0334.1>
- Tsoulis D, Stary B (2005) An isostatically compensated gravity model using spherical layer distributions. *J Geod* 78:418–424. <https://doi.org/10.1007/s00190-004-0404-3>
- Tsoulis D, Wziontek H, Petrovic S (2003) A bilinear approximation of the surface relief in terrain correction computations. *J Geod* 77:338–344. <https://doi.org/10.1007/s00190-003-0332-7>
- Tsoulis D, Novák P, Kadlec M (2009) Evaluation of precise terrain effects using high-resolution digital elevation models. *J Geophys Res Solid Earth.* <https://doi.org/10.1029/2008JB005639>
- Tychonov A, Samarski AA (1964) Partial differential equations of mathematical physics. Holden-day
- Uieda L, Barbosa VCF, Braatenberg C (2016) Tesseroids: forward-modeling gravitational fields in spherical coordinates. *Geophysics* 81:F41–F48. <https://doi.org/10.1190/geo2015-0204.1>
- Van Camp M, de Viron O, Watlet A et al (2017) Geophysics from terrestrial time-variable gravity measurements. *Rev Geophys* 55:938–992
- Van Oosterom A, Strackee J (2007) The solid angle of a plane triangle. *IEEE Trans Biomed Eng.* <https://doi.org/10.1109/tbme.1983.325207>
- Werner R, Scheeres D (1997) Exterior gravitation of a polyhedron derived and compared with harmonic and mascon gravitation representations of asteroid 4769 Castalia. *Celest Mech Dyn Astron* 65:313–344. <https://doi.org/10.1007/BF00053511>
- Woodward DJ (1975) The gravitational attraction of vertical triangular prisms. *Geophys Prospect* 23:526–532. <https://doi.org/10.1111/j.1365-2478.1975.tb01546.x>